

# The N-terminal pre-A region of *Mycobacterium tuberculosis* 2/2HbN promotes NO-dioxygenase activity

Alessandra Pesce<sup>1</sup>, Juan P. Bustamante<sup>2</sup>, Axel Bidon-Chanal<sup>3</sup>, Leonardo Boechi<sup>2</sup>, Darío A. Estrin<sup>2</sup>, Francisco Javier Luque<sup>3</sup>, Anne Sebilo<sup>4</sup>, Michel Guertin<sup>4</sup>, Martino Bolognesi<sup>5,6</sup>, Paolo Ascenzi<sup>7,8</sup> and Marco Nardini<sup>5</sup>

1 Department of Physics, University of Genova, Italy

2 Departamento de Química Inorgánica, Analítica y Química Física/INQUIMAE-CONICET, Facultad de Ciencias Exactas y Naturales, University of Buenos Aires, Argentina

3 Departament de Físicoquímica and Institut de Biomedicina (IBUB), Facultat de Farmàcia, University of Barcelona, Santa Coloma de Gramenet, Spain

4 Department of Biochemistry, Microbiology and Bioinformatics, Laval University, Quebec, Canada

5 Department of Biosciences, University of Milan, Italy

6 CNR-IBF and CIMAINA, University of Milan, Italy

7 Interdepartmental Laboratory of Electron Microscopy, Roma Tre University, Rome, Italy

8 National Institute of Biostructures and Biosystems, Rome, Italy

## Keywords

2/2 hemoglobins; globin dynamics; heme/ligand tunneling; NO dioxygenase; truncated hemoglobins

## Correspondence

M. Nardini, Department of Biosciences, University of Milano, I-20133 Milano, Italy  
Fax: +39 02 5031 4895  
Tel: +39 02 503 14898  
E-mail: marco.nardini@unimi.it

(Received 5 August 2015, revised 9 August 2015, accepted 16 August 2015)

doi:10.1111/febs.13571

A unique defense mechanisms by which *Mycobacterium tuberculosis* protects itself from nitrosative stress is based on the O<sub>2</sub>-dependent NO-dioxygenase (NOD) activity of truncated hemoglobin 2/2HbN (*Mt2/2HbN*). The NOD activity largely depends on the efficiency of ligand migration to the heme cavity through a two-tunnel (long and short) system; recently, it was also correlated with the presence at the *Mt2/2HbN* N-terminus of a short pre-A region, not conserved in most 2/2HbNs, whose deletion results in a drastic reduction of NO scavenging. In the present study, we report the crystal structure of *Mt2/2HbN*-ΔpreA, lacking the pre-A region, at a resolution of 1.53 Å. We show that removal of the pre-A region results in long range effects on the protein C-terminus, promoting the assembly of a stable dimer, both in the crystals and in solution. In the *Mt2/2HbN*-ΔpreA dimer, access of heme ligands to the short tunnel is hindered. Molecular dynamics simulations show that the long tunnel branch is the only accessible pathway for O<sub>2</sub>-ligand migration to/from the heme, and that the gating residue Phe(62)E15 partly restricts the diameter of the tunnel. Accordingly, kinetic measurements indicate that the *k*<sub>on</sub> value for peroxynitrite isomerization by *Mt2/2HbN*-ΔpreA-Fe(III) is four-fold lower relative to the full-length protein, and that NO scavenging by *Mt2/2HbN*-ΔpreA-Fe(II)-O<sub>2</sub> is reduced by 35-fold. Therefore, we speculate that *Mt2/2HbN* evolved to host the pre-A region as a mechanism for preventing dimerization, thus reinforcing the survival of the microorganism against the reactive nitrosative stress in macrophages.

## Abbreviations

2/2Hb, 2-on-2 globin; At2/2AHb3, 2/2AHb3 from *Arabidopsis thaliana*; DLS, dynamic light scattering; FdR, NADH-flavodoxin reductase; ILS, implicit ligand sampling; MD, molecular dynamics; *Mt2/2Hb*, *Mycobacterium tuberculosis* 2/2Hb; *Mt2/2HbN*-ΔpreA, *Mt2/2HbN* deletion mutant devoid of the first 11 amino acids; NOD, nitric oxide dioxygenase; PDB, Protein Data Bank.

**Database**

Coordinates and structure factors have been deposited in the Protein Data Bank under accession number [5AB8](#).

**Introduction**

The ‘truncated’ 2/2 hemoglobins (2/2Hbs) are small oxygen-binding heme proteins identified in bacteria, higher plants and certain unicellular eukaryotes, building a separate cluster within the hemoglobin superfamily. 2/2Hbs display amino acid sequences that are 20–40 residues shorter than (non)vertebrate Hbs, to which they are loosely related by sequence similarity (sequence identity < 20%) [1–4].

The 2/2Hb protein fold has been described as consisting of a simplified version of the ‘classical’ globin fold typical of sperm whale Mb (a 3-on-3  $\alpha$ -helical sandwich) [5]. The topology of the 2/2Hb fold is characterized by a 2-on-2  $\alpha$ -helical sandwich, based on four  $\alpha$ -helices, corresponding to the B/E and G/H antiparallel helix pairs of the classical globin fold, which surround and shield the heme group from the solvent [6–9].

Based on amino acid sequence analysis, three 2/2Hbs phylogenetic groups (groups I, II and III, whose members are designated by the N, O and P suffixes, respectively) were recognized, with the proteins being orthologous within each group and paralogues across the groups. In some cases, 2/2Hbs from more than one group can coexist in the same organism, indicating the diversification of their functions [2].

In general, members of the 2/2Hb family are monomeric or dimeric proteins, characterized by medium to very high oxygen affinity [10]. Some of the organisms hosting 2/2Hbs are pathogenic bacteria; others perform photosynthesis, fix nitrogen or may display distinctive metabolic capabilities. Nevertheless, limited functional information is currently available for these proteins. Examples of proposed functions include nitric oxide detoxification, protection from reactive oxygen and nitrogen species, dioxygen scavenging, and sulfide binding [11–15]. Most of the functional analyses have been reported for mycobacterial 2/2Hbs that have been implicated in scavenging of reactive nitrogen species [1,2,16] produced by activated macrophages expressing inducible NO-synthase [17–22]. For example, *Mycobacterium tuberculosis* 2/2HbN (*Mt2/HbN*) is endowed with a potent nitric-oxide dioxygenase (NOD) activity; the protein has been found to relieve nitrosative stress [10,11,23], enhancing the survival of the heterologous host *Salmonella enterica* serovar

*typhimurium* within macrophages [24]. It has also been demonstrated that disruption of the *glbN* gene, encoding 2/2HbN, in *Mycobacterium bovis* bacillus Calmette–Guérin causes a dramatic reduction in the NO-consuming activity of stationary phase cells, resulting in marked NO-induced inhibition of aerobic respiration relative to the wild-type cells [11]. Indeed, the NOD function appears to be more common and ancient than the classic O<sub>2</sub> transport-storage function, or any other function, within the Hb superfamily [25]. X-ray crystallographic and computational studies have highlighted the relationship between structure and NOD function of key residues in *Mt2/HbN* [26–29]. Moreover, a number of experimental studies have been devoted to the spectroscopic and structural characterization of binding of diatomic ligands (CO, O<sub>2</sub>, NO and cyanide) to *Mt2/HbN* [10,30–33]. These studies indicate that ligand binding is largely controlled by a pair of interacting amino acids, Tyr(33)B10 and Gln(58)E11, which are present in the heme distal site and participate in hydrogen bonding with the heme-bound O<sub>2</sub> [10,26,30,31]. On the other hand, analysis of the *Mt2/HbN* three-dimensional structure has shown that the protein, similar to other members of the 2/2HbN group I, is characterized by the presence of a protein matrix tunnel system, which connects the protein surface to an inner region merging with the heme distal site [34,35]. These data are in keeping with the accumulating evidence indicating that oxygen access in proteins (not only globins, but also flavoprotein oxidases, cytochrome *c* oxidases, [NiFe]-hydrogenase and others) is guided and controlled [36–38]. O<sub>2</sub> diffusion through the protein matrix can occur on the (tens of) nanosecond time scale, based on dynamic fluctuations of the protein structure and (transient) inner cavities. Although such processes, often explored through molecular dynamics (MD) and O<sub>2</sub>-based quenching of fluorescence experiments [39,40], show that diffusion of O<sub>2</sub> is dynamically possible along several different paths, O<sub>2</sub> prolonged residence in (transient) hydrophobic cavities, separated by free energy barriers of 2–5 kcal·mol<sup>-1</sup>, is a commonly observed feature. Static protein matrix tunnels, with entry points at the protein surface, such as those identified in *Mt2/HbN*, may facilitate fast ligand diffusion and add regulatory

gating mechanisms on specific lining residues. Moreover, a clearly identified tunnel, as opposed to paths through a densely packed protein matrix, may host several O<sub>2</sub> molecules at the same time, thus increasing critically the local concentration of the ligand.

*Mt2/2HbN* is characterized by a tunnel system composed of two approximately orthogonal branches converging at the heme distal site from two distinct protein surface access sites. A 20-Å long tunnel branch connects the protein region nestled between the AB and GH hinges to the heme distal site, whereas a short tunnel branch of approximately 8 Å connects an opening in the protein structure, between G- and H-helices, to the heme [34]. Residues lining both tunnel branches are hydrophobic and are substantially conserved throughout group I 2/2Hbs [2].

NMR spectroscopy and MD data indicate that rigidity of the B, E, G and H helices, which form the 2/2Hb helical core, may prevent the optimization of internal side-chain van der Waals interactions that would otherwise result in tighter side-chain packing and the loss of tunnels. At the same time, the free internal volume of tunnels, coupled with thermal fluctuations, may allow conformational flexibility of residues lining the tunnels, a mandatory property for diatomic ligand migration [28,41,42]. In particular Phe(62)E15, a tunnel long branch residue, can adopt two conformations where its phenyl side chain may block the tunnel branch (the so-called closed state) or not (the open state) [26,34]. However, the results of a recent study suggest that the so-called closed state does not fully prevent transit of ligands [43].

Migration of O<sub>2</sub> and NO to the *Mt2/2HbN* distal heme cavity has been proposed to be supported by a dual-path mechanism, where Phe(62)E15 primarily adopts the closed conformation in deoxygenated *Mt2/2HbN*; hence, O<sub>2</sub> would enter the protein via the short tunnel branch. Conversely, transitions between open and closed forms of the Phe(62)E15 gate would facilitate entrance of the second ligand (NO) via the long tunnel branch in oxygenated *Mt2/2HbN* [27,44–47]. On the other hand, different MD simulations suggested that the short tunnel branch would preferentially be used by NO to reach the distal heme pocket. Such a preference was ascribed to the hydrophobic funnel-shaped tunnel entrance, covering a large area extending far from the tunnel entrance [41].

Strikingly, the *Mt2/2HbN* NOD activity has been correlated with the presence of the *Mt2/2HbN*-specific pre-A short helix (Fig. 1). Deletion of the pre-A region from the *Mt2/2HbN* drastically reduces its ability to scavenge NO (present study), whereas its insertion at the N-terminus of *Mycobacterium smegmatis* 2/2HbN,

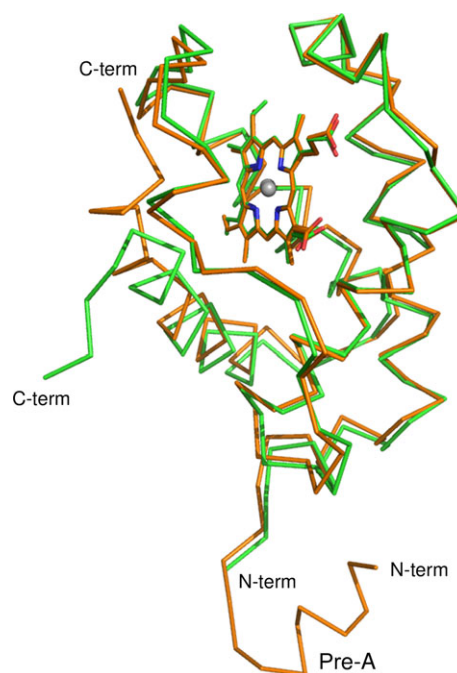


**Fig. 1.** The *Mt2/2HbN-ΔpreA* tertiary structure.  $\alpha$ -trace overlay of *Mt2/2HbN-ΔpreA* (green) and *Mt2/2HbN* (orange). The locations of the N- and C-termini of *Mt2/2HbN-ΔpreA* and *Mt2/2HbN*, as well as of the pre-A helix in *Mt2/2HbN*, are indicated.

which lacks the pre-A region, improved its NOD activity [29]. MD simulations on a theoretical model where the pre-A motif was deleted from the full-length *Mt2/2HbN* suggested that excision of the pre-A motif would trigger distinct changes in protein dynamics, hampering the open/closed transitions of the Phe(62)E15 gate, and trapping the tunnel long branch in a closed conformation, thus hindering migration of diatomic ligands toward the heme distal site [29]. Furthermore, deletion of the pre-A region was shown to abrogate the heme iron reduction by NADH-flavodoxin reductase (FdR), thus signifying its involvement in the intermolecular interactions between *Mt2/2HbN* and FdR that are needed for HbN recycling during NO deoxygenation [48].

In consideration of the peculiar structural and functional properties displayed by *Mt2/2HbN*, we focused our attention on the roles played by the N-terminal pre-A region, which is scarcely conserved in 2/2Hbs. Specifically, we solved the crystal structure of a deletion mutant devoid of the first 11 amino acids (hereafter named *Mt2/2HbN-ΔpreA*). Furthermore, the peroxynitrite scavenging of *Mt2/2HbN-ΔpreA-Fe(III)* and the NO detoxification properties of *Mt2/2HbN-ΔpreA-Fe(II)-O<sub>2</sub>* were analyzed. Finally, MD simulations allowed us to explore the dynamical properties of

the *Mt2/2HbN-ΔpreA* variant, with the aim of gaining insight into the potential regulatory role of the pre-A region on the NO-detoxifying ability of *Mt2/2HbN*.

## Results

### Crystal structure of *Mt2/2HbN-ΔpreA*

Ferric *Mt2/2HbN-ΔpreA* crystallizes in the hexagonal space group *P6<sub>1</sub>22* (Table 1), with one protein molecule in the asymmetric unit. The structure was refined at a resolution of 1.53 Å to final  $R_{\text{factor}}$  and  $R_{\text{free}}$  values of 14.0% and 20.9%, respectively (Table 1). The tertiary structure of *Mt2/2HbN-ΔpreA* in its backbone closely matches that of full-length *Mt2/2HbN* [26], displaying a RMSD value of 0.65 Å, as calculated for 105 C $\alpha$  atom pairs (residues 12–117) (Fig. 1). This result is in accordance with previous CD data indicating that the deletion of the pre-A region does not produce major changes in the protein overall structure, nor negatively affect its structural integrity [29]. However, the analysis of the *Mt2/2HbN-ΔpreA* crystal

structure shows that specific differences are present in the backbone conformation of the second half of the H-helix, which shifts closer to the E-helix by approximately 1.6 Å [C $\alpha$ -C $\alpha$  distance as measured between Phe(62)E15 and Ile(119)H14], relative to the full-length protein (Fig. 2A,B). Moreover, the C-terminal segment of the protein (residues 125–128) adopts an orientation opposite to that observed in the full-length protein (Figs 1 and 2A,B).

The deletion of the N-terminal region of ferric *Mt2/2HbN-ΔpreA* does not alter the overall structure of the heme-binding pocket (Fig. 2C,D). Notably, a formate molecule (from the crystallization solution) is bound to the heme-Fe(III) atom, with a coordination bond to the formate O1 atom of 1.86 Å. The second oxygen atom (O<sub>2</sub>) of the formate molecule is hydrogen bonded to Tyr(33)B10 OH (2.50 Å). Such a ligand binding mode is very similar to that observed for cyanide in *Mt2/2HbN-Fe(III)* [Protein Data Bank (PDB) code: [1RTE](#)] (Fig. 2C), and for O<sub>2</sub> in *Mt2/2HbN-Fe(II)* (PDB code: [1IDR](#)) (Fig. 2D). Nevertheless, a minor backbone shift is present (range 0.5–1.5 Å) in the CE hinge region, at residues 48–52.

**Table 1.** Data collection and refinement statistics.

Data collection	
Space group	<i>P6<sub>1</sub>22</i>
Cell dimensions	
<i>a</i> , <i>b</i> , <i>c</i> (Å)	43.2, 46.2, 212.9
$\alpha$ , $\beta$ , $\gamma$ (°)	90.0, 90.0, 120.0
Resolution (Å)	53.23–1.53 (1.61–1.53) <sup>a</sup>
Number of reflections	293 750
Unique reflections	18 944
$R_{\text{merge}}$ (%) <sup>b</sup>	10.1 (40.3)
$I/\sigma(I)$	15.7 (5.8)
Completeness (%)	99.9 (99.6)
Multiplicity	15.5 (15.9)
Refinement statistics	
$R_{\text{factor}}/R_{\text{free}}$ (%) <sup>c</sup>	14.0/20.9
Protein residues	117 (residues 12–128)
Heme groups	1
Formate	1
Glycerol	2
Acetate	1
Water molecules	148
RMSD from ideality	
Bond lengths (Å)	0.010
Bond angles (°)	1.5
Ramachandran plot (%)	
Most favored	99.1
Additionally allowed	0.9
Disallowed regions	0.0

<sup>a</sup> Highest resolution shell parameters are shown in parentheses.

<sup>b</sup>  $R_{\text{merge}} = \sum_h \sum_i |I_{hi} - \langle I_h \rangle| / \sum_h \sum_i I_{hi}$ . <sup>c</sup>  $R_{\text{factor}} = \sum_h \|F_{\text{obs}} - F_{\text{calc}}\| / \sum_h |F_{\text{obs}}|$ , with  $F_{\text{obs}}$  and  $F_{\text{calc}}$  being the observed and calculated structure factor amplitudes, respectively.

### Dimerization and heme accessibility

Dynamic light scattering (DLS) experiments on *Mt2/2HbN-ΔpreA* show that the protein is mostly monodisperse, with 99.7% of the scattering mass having a hydrodynamic radius of 2.3 nm, corresponding to an estimated molecular mass of approximately 23 kDa, almost matching that of a dimeric species (Fig. 3). Accordingly, packing of protein molecules in the crystal shows a symmetrical *Mt2/2HbN-ΔpreA* homodimer, whose association interface is contributed mostly by residues belonging to the G- and H-helices, the FG hinge and the C-terminus (Fig. 4A,B). The stability of such a quaternary assembly is suggested by the large buried contact area (2041 Å<sup>2</sup> for each subunit of the dimer, corresponding to 36.7% of the total accessible surface area) and the estimated dissociation free energy of 13.3 kcal·mol<sup>-1</sup> (with eight hydrogen bonds across the interface), as calculated by PISA [49].

The most striking consequence of *Mt2/2HbN-ΔpreA* dimerization is that the access to the short tunnel branch (located between the G- and H-helices) is sterically hindered, with residues at the N-terminus of the G-helix of one subunit building a barrier between the solvent and the short tunnel branch of the facing subunit (Fig. 4C, D). By contrast, the long tunnel branch entrance, nestled between the AB and GH hinges, remains solvent accessible in the dimer; nevertheless, relative to the full-length protein, the diameter of the tunnel is more

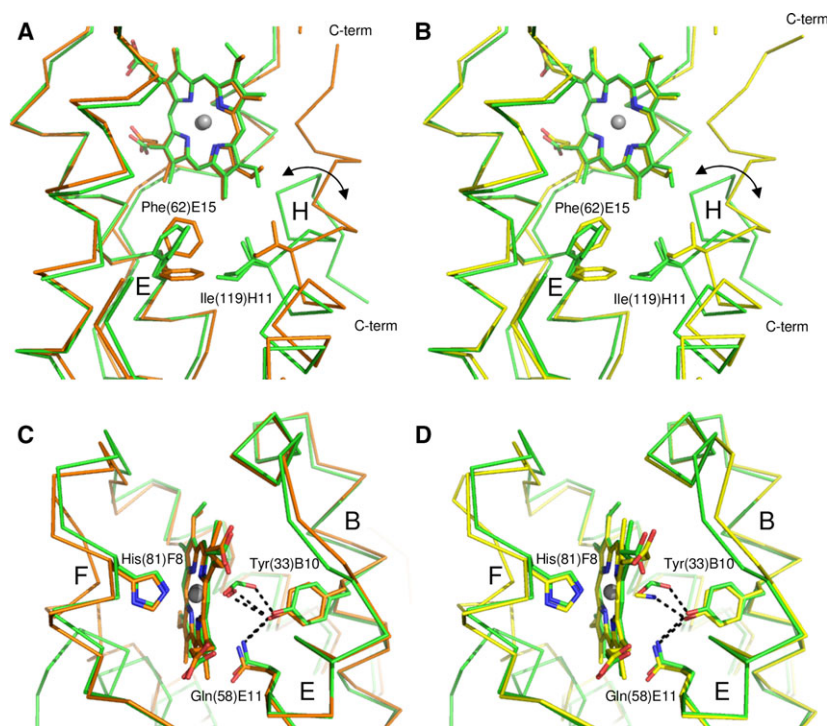


**Fig. 2.** Long branch tunnel and heme distal site in *Mt2/2HbN-ΔpreA*. Superimposition of *Mt2/2HbN-ΔpreA*(III)-formate (green) to (A, C) *Mt2/2HbN*(III)-cyanide (orange) and (B, D) *Mt2/2HbN*(II)-O<sub>2</sub> (yellow). (A, B) The position and the conformation of the Phe(62)E15 side chain, gating the long branch tunnel, is highlighted. (C, D) Residues lining the heme distal pocket and the bound ligands are indicated and shown in stick representation. The proximal His(81)F8 residue is also shown. Relevant secondary structure elements and amino acid residues are labeled (using their three-letter codes, the sequence numbering and the topological site that they occupy within the globin fold). Hydrogen bonds are indicated by dashed lines.

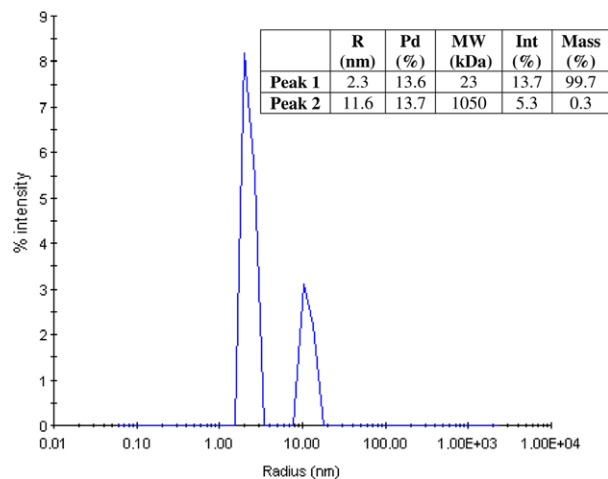


**Fig. 3.** DLS measurements. Calculated size distribution for the correlation curve associated with the DLS measurements. The inset provides a per peak breakdown of the size distribution, including the mean size radius (R), polydispersity (Pd, SD of the peak), estimated molecular weight (MW), intensity and mass contributions to the signal.

restricted at the Phe(62)E15 gating site as a result of a closer positioning of the H- and E-helices (Fig. 2A,B). The side chain orientation of Phe(62)E15, which would gate the long tunnel branch, resembles one of the conformations observed in the crystal structures of *Mt2/2HbN-Fe*(III)-cyanide (PDB code: [1RTE](#)) and *Mt2/2HbN-Fe*(II)-O<sub>2</sub> (PDB code: [1IDR](#)) (Fig. 2A,B). Indeed, in the crystal structure of the full-length *Mt2/2HbN*, two Phe(62)E15 conformations co-exist: one with the Phe side chain running almost parallel to the long tunnel branch (dihedral  $\chi_1 = -91^\circ$ ) and the second with the side chain oriented orthogonally to the tunnel axis (dihedral  $\chi_1 = -155^\circ$ ) [26].

MD simulations have highlighted frequent transitions between the two conformations in oxygenated *Mt2/2HbN*, which would underline the availability of the tunnel long branch to migration of gaseous ligands towards the heme cavity [27,28,44,46]. In this respect, it is interesting to note that the high resolution (1.53 Å) achieved for the *Mt2/2HbN-ΔpreA* structure allows unambiguous modeling of two slightly different conformers (both with 0.50 occupancy) for the Phe(62)

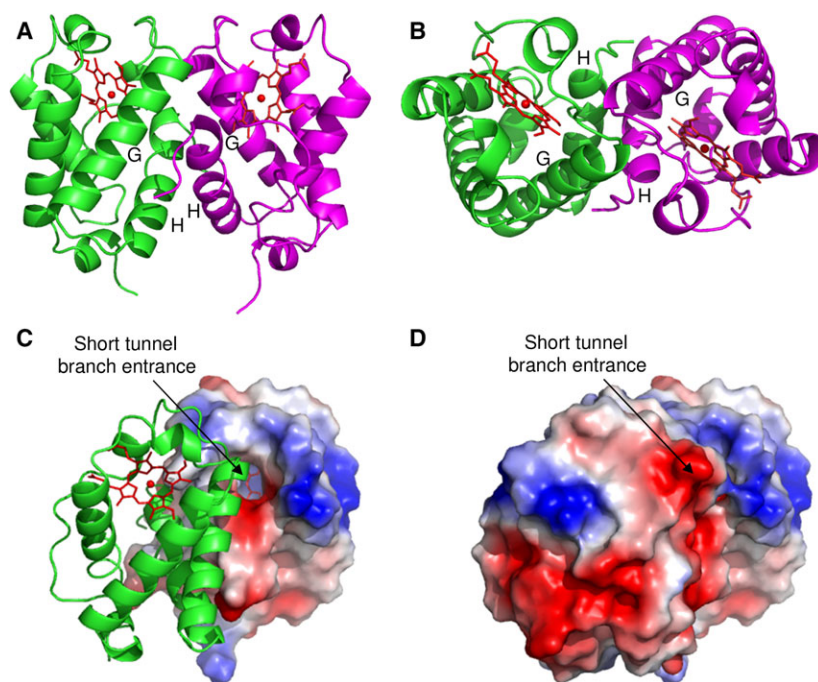


**Fig. 4.** The *Mt2/2HbN-ΔpreA* quaternary structure. Ribbon representation of *Mt2/2HbN-ΔpreA* dimeric assembly. The dimer subunits are represented in green and magenta, in side view (A) and top view (B). Helices at the dimeric interface are labelled. (C, D) Electrostatic surface of *Mt2/2HbN-ΔpreA*. Blue and red highlight positively- and negatively-charged surfaces, respectively. The entrance of the short tunnel branch is indicated in (C), where the surface of one dimeric subunit is omitted. (D) Where the surfaces of both subunits are shown, the entrance appears to be completely hindered. The heme group is always shown in red.

E15 side chain, confirming the dynamical (gating) nature of this residue phenyl ring. In particular, in the two conformations, the  $\chi_1$  dihedral angle is unchanged ( $-77^\circ$  and  $-76^\circ$ , respectively), although the  $\chi_2$  angle varies ( $32^\circ$  and  $5^\circ$ , respectively), indicating that the long tunnel branch is partly hindered by the Phe(62)E15 aromatic moiety. The double conformation of the Phe(62)E15 side chain is coupled with the double conformation of residue Ile(119)H11, which faces Phe(62)E15 on the H-helix (Fig. 2A,B). Thus, in *Mt2/2HbN-ΔpreA*, the dimerization appears to restrict the diameter of the tunnel at the Phe(62)E15 site, either directly by shifting the H-helix, and indirectly by selecting, via Ile(119)H11, a Phe(62)E15 conformation that partly hinders the tunnel section. Indeed, previous NMR studies have revealed the presence of localized motions in the microsecond to millisecond time scale that could be assigned to a translational movement of the *Mt2/2HbN-ΔpreA* G-helix or of the neighboring H-helix, thus having implications for the dynamics of the tunnels, the heme distal site and ligand diffusion, as well as for the protein kinetic properties [42].

The symmetrical *Mt2/2HbN-ΔpreA* homodimer architecture cannot be achieved by full-length *Mt2/2HbN* as a result of the different structure of the C-terminal region, which would collide with the FG region of the facing subunit (in full-length *Mt2/2HbN*) (Fig. 5A). Although, in the crystal structure of *Mt2/2HbN*, the pre-A region is located away from the *Mt2/2HbN-ΔpreA* homodimer interface (Fig. 5A),

such a location is imposed by crystal packing, and thus is not truly significant. Indeed, previous MD simulations and NMR studies showed that the pre-A helix is very mobile and unstable in solution, exploring a wide range of conformers as a result of the flexibility of the pre-A-A hinge and a certain tendency to unfold [29,42]. Hence, it cannot be excluded that the N-terminal pre-A helix plays also a direct role in hampering the dimerization of the full-length protein. In particular, the pre-A helix may fold back towards the H-helix, thus potentially interfering with the dimeric association interface reported in the present study for *Mt2/2HbN-ΔpreA*. A similar situation has been reported for the nonsymbiotic plant hemoglobin 2/2AHb3 from *Arabidopsis thaliana* (*At2/2AHb3*), one of the few 2/2Hbs hosting an extended pre-A region (PDB code: [4C0N](#)) [50]. In *At2/2AHb3*, the pre-A region folds against the H-helix, thus shielding from the solvent the G- and H-helices, which, in *Mt2/2HbN-ΔpreA*, build up the dimerization interface (Fig. 5B).

### MD simulation

The effect of pre-A region deletion on the dynamical behavior of the dimeric form of the deoxygenated and oxygenated protein species was examined by means of MD simulations. For the oxygenated *Mt2/2HbN-ΔpreA*, three MD simulation replicas were run. In all of them, the structure of each subunit within the dimer

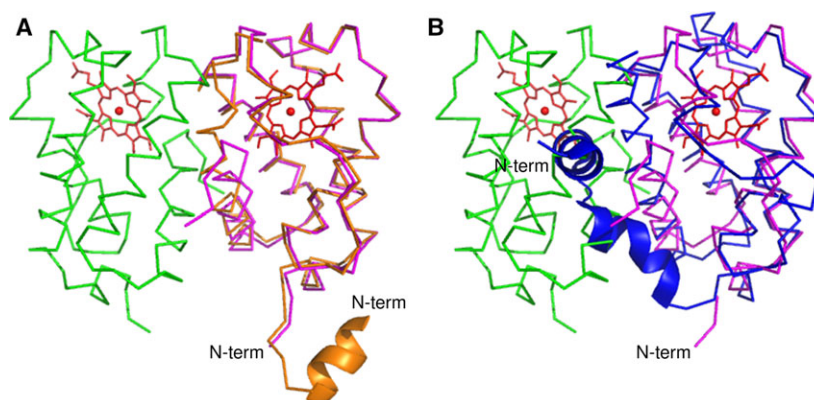


**Fig. 5.** *Mt2/2HbN-ΔpreA* dimer and related proteins. Superimposition of *Mt2/2HbN-ΔpreA* dimer (green and magenta) to (A) *Mt2/2HbN* (orange) and (B) *At2/2AHb3* (blue) monomers. The N-terminal helical region of *Mt2/2HbN* and *At2/2AHb3* is shown in ribbon representation.

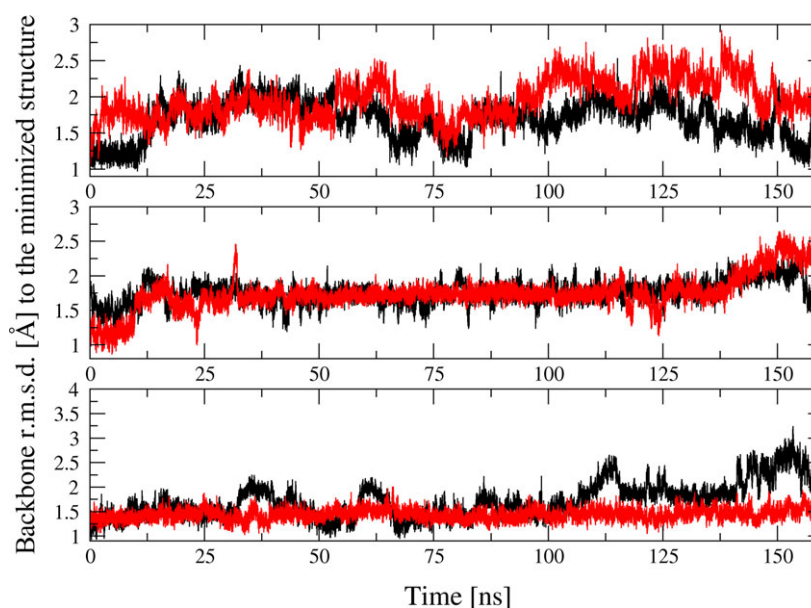


**Fig. 6.** RMSD of the protein backbone for each subunit in the *Mt2/2HbN-ΔpreA* dimer. RMSD data determined from MD simulations for monomers A and B are shown in black and red, respectively.

is well preserved along the trajectory, with RMSD values typically  $< 2 \text{ \AA}$  (Fig. 6).

Conformational analysis of the Phe(62)E15 gate reveals the occurrence of transitions between open and closed states in both subunits of the dimer, with a slightly higher frequency in subunit A than in subunit B (Fig. 7). Implicit ligand sampling (ILS) calculations corroborate the opening of the long tunnel branch connecting the distal cavity to the solvent, as noted by the continuous isosurface that appears along the tunnel branch at a favorable interaction energy level of  $-1 \text{ kcal}\cdot\text{mol}^{-1}$  (Fig. 8A) in the three replicas. Taking into account that the dimeric structure of *Mt2/2HbN-ΔpreA* sterically impedes the access of gaseous ligands to the short tunnel branch (Fig. 4C,D), the MD simulations show that, in the deletion mutant, the long tunnel branch is endowed with sufficient dynamics to grant access to the distal site from the solvent region, partly compensating for the observed occlusion of the short

tunnel branch. Interestingly, the ILS results also show a clear connection between the short tunnels present in each monomer, suggesting that gaseous ligands might move from one monomer to the other using this connection pathway (Fig. 8B). Upon inspection of the ILS maps, the narrowest part of the tunnel system appears to be located at the junction between long and short tunnel branches, delimited by residues Val(94)G8, Ala(95)G9 and Ile(119)H11. The diameter of the tunnel bottleneck is estimated to be approximately  $2.5 \text{ \AA}$ , suggesting that the thermal fluctuations should *a priori* enable the passage of gaseous ligands. Noteworthy, Val(94)G8 has been shown to play a key role in the control of ligand association in truncated Hbs [43].

To check the accessibility of a diatomic ligand to the heme distal site through the long tunnel branch, a 150-ns MD simulation was performed for the deoxygenated form of the dimeric *Mt2/2HbN-ΔpreA*, starting with an oxygen molecule free in the solvent. The

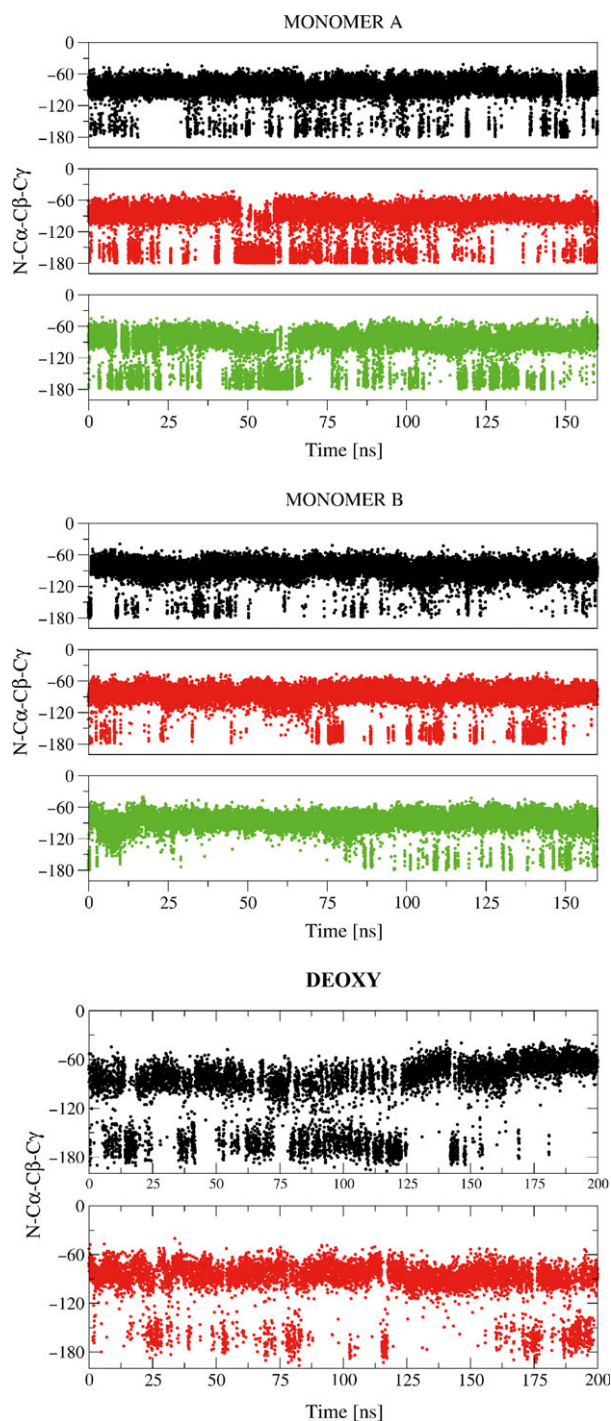


**Fig. 7.** Open/close conformational transitions in Phe(62)E15 gate. Representation of the conformational transitions of the Phe(62)E15 side chain for monomer A (top) and B (middle) in the three independent simulations run for oxygenated *Mt2/2HbN-ΔpreA* dimer (the three MD simulations are shown in black, red and green, respectively), as well as in the single MD simulation run for deoxygenated *Mt2/2HbN-ΔpreA* dimer (bottom; transitions in monomer A and B are shown in black and red, respectively).

protein fold of the two subunits was stable during the MD simulation (data not shown). Inspection of the ligand trajectory confirmed that the only accessible pathway for  $O_2$  migration from and to the solvent is the long tunnel branch, whereas, once in the protein inner region, the gaseous ligand is able to visit both tunnels (Fig. 9A). Interestingly, the  $O_2$  ligand is able to visit the heme cavity of one *Mt2/2HbN-ΔpreA* chain even when access to the dimeric protein has occurred through the opposite monomer, thus confirming the transfer between the two monomers through the junction linking their short tunnels. Indeed, the  $O_2$  ligand enters or escapes from (or to) the solvent several times during the time scale of the simulations, using either one of the two long tunnel branches in the dimeric species (Fig. 9C). A similar oxygen-free simulation was also performed using the *Mt2/2HbN* monomer, where the oxygen molecule entered and escaped several times using both long and short tunnel branches (Fig. 9B,C).

Even though, in the deoxygenated form of dimeric *Mt2/2HbN-ΔpreA*, the Phe(62)E15 gate exhibits transitions between the open and closed conformational states (Fig. 7), it is worth noting that ligand migration appears to be less favored in the N-terminal deletion mutant than in the full-length protein. This is indicated by the gaseous ligand distribution maps in the protein interior, which show a much higher ligand occupancy of the tunnel in the wild-type protein (Fig. 9B), whereas a decreased ligand occupancy around the Phe(62)E15 gate is found in the *Mt2/2HbN-ΔpreA* protein (Fig. 9A).

Overall, the MD analyses suggest that in the *Mt2/2HbN-ΔpreA* dimer access of the ligand to the protein interior occurs through the long tunnel branch, whereas the accessibility to the heme cavity through the short tunnel branch is hindered by dimerization, with the short tunnel branches of two facing chains being connected. Furthermore, ligand migration through the long tunnel branch is less favored compared to the full-length protein, a trend that would lead to a reduction in the dioxygenase activity of *Mt2/2HbN-ΔpreA*.

### Kinetics of peroxynitrite isomerization by *Mt2/2HbN-ΔpreA-Fe(III)*

Kinetics of peroxynitrite isomerization was fitted to a single-exponential decay for more than  $92 \pm 8\%$  of its course according to Eqn (1) (see Materials and methods), thus indicating that no intermediate species [e.g. *Mt2/2HbN-ΔpreA-Fe(III)-OONO*] accumulate(s) in the course of peroxynitrite isomerization, as previously

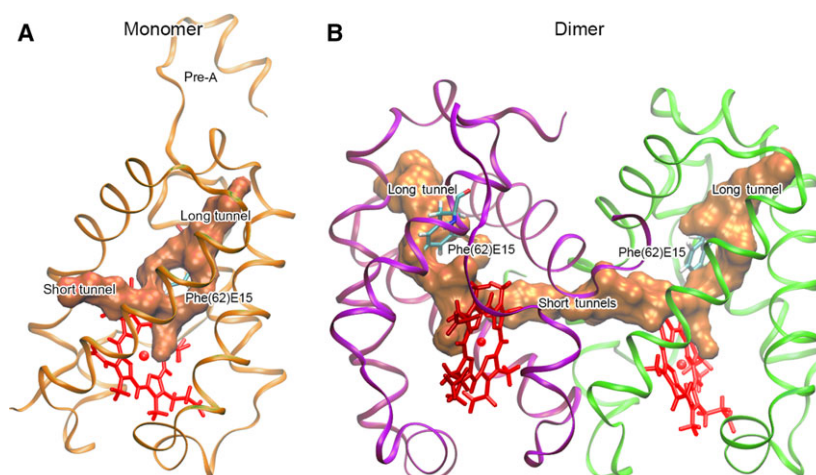


**Fig. 8.** Accessible ligand migration pathways in *Mt2/2HbN-ΔpreA*. Inner tunnel in the protein matrix determined from ILS calculations using  $O_2$  as a molecular probe. (A) The steric hindrance exerted by the Phe(62)E15 gate is visible in the bifurcated path formed around this residue in the representation obtained for each monomer (similar plots are obtained for the two monomers). (B) The structural arrangement of the dimer enables the junction of the short tunnels at the interface, which should allow migration of gaseous diatomic ligands between the two monomers. The isocontour used to display the inner tunnel corresponds to an energy value of  $-1 \text{ kcal}\cdot\text{mol}^{-1}$ .

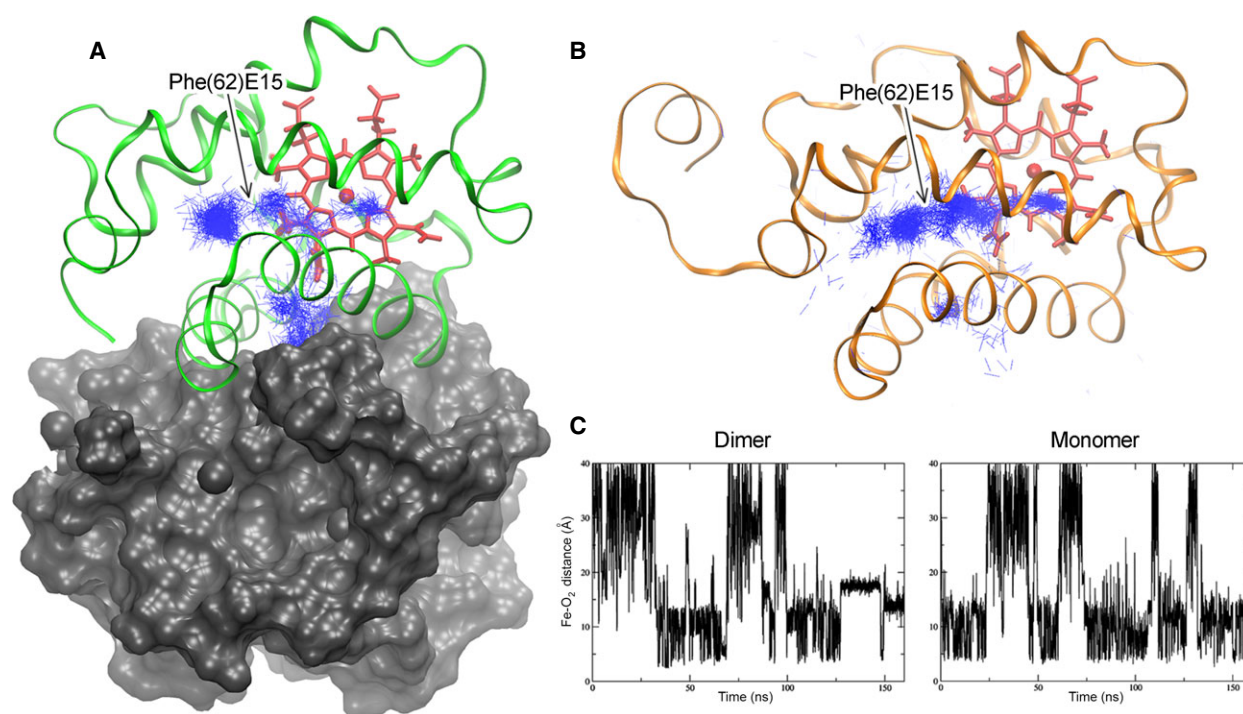


**Fig. 9.**  $O_2$  migration from unbiased MD simulations.  $O_2$  ligand migration along possible pathways in (A) the dimeric *Mt2/2HbN-ΔpreA* and (B) the monomeric full-length protein. The pathways denote the position of  $O_2$  along the trajectories. In the dimeric *Mt2/2HbN-ΔpreA*, migration through the short tunnel branch leads to the facing monomer, whereas, in the monomeric protein, full-length protein would lead to bulk solvent. (C) Time evolution of the distance from  $O_2$  to the heme Fe-atom in the dimeric *Mt2/2HbN-ΔpreA* and monomeric full-length protein.

reported for full-length *Mt2/2HbN-Fe(III)* [51]. In particular, the formation of the transient *Mt2/2HbN-ΔpreA-Fe(III)-OONO* species represents the rate-limit-

ing step in catalysis, being slower by at least one order of magnitude than its conversion to *Mt2/2HbN-ΔpreA-Fe(III)* and  $NO_3^-/NO_2^-$ .

The observed rate constant for *Mt2/2HbN-ΔpreA*-Fe(III)-catalyzed isomerization of peroxyxynitrite (i.e.  $k$ ) increases linearly with the *Mt2/2HbN-ΔpreA*-Fe(III) concentration (Fig. 10). Values of the second-order rate constant for *Mt2/2HbN-ΔpreA*-Fe(III)-catalyzed isomerization of peroxyxynitrite (i.e.  $k_{on}$ ) and of the first-order rate constant for peroxyxynitrite isomerization in the absence of *Mt2/2HbN-ΔpreA*-Fe(III) (i.e.  $k_0$ ) are  $(1.4 \pm 0.2) \times 10^4 \text{ M}^{-1}\cdot\text{s}^{-1}$  (corresponding to the slope of the linear plot) and  $0.29 \pm 0.03 \text{ s}^{-1}$  (corresponding to the y-intercept of the linear plot), respectively. Both values are in good agreement with those reported in the literature for ferric heme proteins [51–62].

Values of  $k_{on}$  for peroxyxynitrite isomerization by ferric heme proteins ranges between  $0.9 \times 10^4 \text{ M}^{-1}\cdot\text{s}^{-1}$  and  $5.8 \times 10^6 \text{ M}^{-1}\cdot\text{s}^{-1}$  (Table 2), reflecting the coordination of the heme-Fe(III) atom, the peroxyxynitrite accessibility to the heme-Fe(III) catalytic center and the Lewis acidity of the heme-Fe(III) atom. The  $k_{on}$  value for peroxyxynitrite *Mt2/2HbN-ΔpreA*-Fe(III) ( $1.4 \times 10^4 \text{ M}^{-1}\cdot\text{s}^{-1}$ ) is four-fold lower than that reported for full-length *Mt2/2HbN*-Fe(III) ( $6.2 \times 10^4 \text{ M}^{-1}\cdot\text{s}^{-1}$ ) [51] (Table 2), even though the distal site environment of the heme Fe(III) atom is structurally conserved in *Mt2/2HbN-ΔpreA* and *Mt2/2HbN* (Fig. 2). Thus, the measured lower reactivity for *Mt2/2HbN-ΔpreA*-Fe(III) could be ascribed to reduced peroxyxynitrite accessibility to the heme-Fe(III)

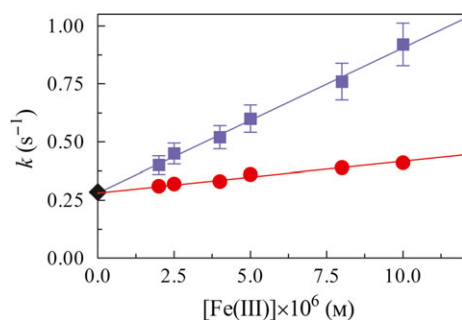


**Fig. 10.** Peroxyxynitrite isomerization by *Mt2/2HbN-ΔpreA*-Fe(III). Dependence of the pseudo-first-order rate constant for peroxyxynitrite isomerization (i.e.  $k$ ) on the *Mt2/2HbN-ΔpreA*-Fe(III) (red circles) and *Mt2/2HbN*-Fe(III) (blue squares) concentration, at pH 7.0 and 20.0 °C. The black symbol on the ordinate indicates the average value of  $k_0$  obtained in the absence of *Mt2/2HbN-ΔpreA*-Fe(III) and *Mt2/2HbN*-Fe(III). The continuous lines were calculated according to Eqn (2) (see Materials and methods) with the parameters: *Mt2/2HbN-ΔpreA*-Fe(III) –  $k_{on} = 1.4 \times 10^4 \text{ M}^{-1}\cdot\text{s}^{-1}$  and  $k_0 = 0.29 \text{ s}^{-1}$ ; and *Mt2/2HbN*-Fe(III) –  $k_{on} = 6.2 \times 10^4 \text{ M}^{-1}\cdot\text{s}^{-1}$  and  $k_0 = 0.28 \text{ s}^{-1}$ . The peroxyxynitrite concentration was  $5.0 \times 10^{-5} \text{ M}$ . Data for *Mt2/2HbN*-Fe(III)-catalyzed isomerization of peroxyxynitrite were obtained from Ascenzi *et al.* [51]. Where not shown, the SD is smaller than the symbol.

catalytic center resulting from sterical hindering of the short tunnel described by the crystal structure (Fig. 4). Moreover, a lower ligand migration capability through the long tunnel branch in the ferric dimer could also be a contributing factor, as suggested by the MD simulations of deoxygenated *Mt2/2HbN-ΔpreA*.

### Kinetics of NO scavenging by *Mt2/2HbN-ΔpreA*-Fe(II)-O<sub>2</sub>

Kinetics of NO scavenging was fitted to a single-exponential decay for more than  $86 \pm 12\%$  of its course according to Eqn (3). This suggests that no intermediate species accumulate(s) in the course of NO

**Table 2.** Peroxyxynitrite scavenging by ferric heme proteins.

Heme protein	$k_{on} (\text{M}^{-1}\cdot\text{s}^{-1})$
<i>Methanosarcina acetivorans</i> protoglobin	$3.8 \times 10^4$
Cys101(E20)Ser mutant <sup>a</sup>	
<i>M. tuberculosis</i> 2/2 -HbN <sup>b</sup>	$6.2 \times 10^4$
<i>M. tuberculosis</i> 2/2HbN-ΔpreA <sup>c</sup>	$1.4 \times 10^4$
<i>Pseudoalteromonas haloplanktis</i> TAC125 2/2-HbO <sup>d</sup>	$2.9 \times 10^4$
Horse heart Mb <sup>e</sup>	$2.9 \times 10^4$
Sperm whale Mb <sup>f</sup>	$1.6 \times 10^4$
Sperm whale Mb His64(E7)Ala mutant <sup>f</sup>	$5.8 \times 10^6$
Sperm whale Mb His64(E7)Asp mutant <sup>f</sup>	$4.8 \times 10^6$
Sperm whale Mb His64(E7)Leu mutant <sup>f</sup>	$5.7 \times 10^4$
Sperm whale Mb Phe43(CD1)Trp/His64(E7)Leu mutant <sup>f</sup>	$5.2 \times 10^4$
Sperm whale Mb His64(E7)Tyr/His97(F8)Gly mutant <sup>f</sup>	$9.0 \times 10^3$
Human Hb <sup>g</sup>	$1.2 \times 10^4$
Human serum heme-albumin <sup>h</sup>	$4.1 \times 10^5$
Ibuprofen-bound human serum heme-albumin <sup>i</sup>	$3.5 \times 10^4$
Truncated human serum heme-albumin <sup>j</sup>	$4.3 \times 10^5$
Ibuprofen-bound truncated human serum heme-albumin <sup>k</sup>	$5.8 \times 10^4$
Cardiolipin-bound horse heart cytochrome <i>c</i> <sup>l</sup>	$3.2 \times 10^5$
Carboxymethylated-horse heart cytochrome <i>c</i> <sup>m</sup>	$6.8 \times 10^4$
Cardiolipin-bound carboxymethylated-horse heart cytochrome <i>c</i> <sup>m</sup>	$5.3 \times 10^5$
<i>Fusarium oxysporum</i> cytochrome P450 NO reductase <sup>n</sup>	$\sim 5 \times 10^5$

<sup>a</sup> pH 7.4 and 20.0 °C [62]. <sup>b</sup> pH 7.0 and 20.0 °C [51]. <sup>c</sup> pH 7.0 and 20.0 °C. Present study. <sup>d</sup> pH 7.0 and 20.0 °C [61]. <sup>e</sup> pH 7.0 and 20.0 °C [53]. <sup>f</sup> pH 7.5 and 20.0 °C [54]. <sup>g</sup> pH 7.5 and 20.0 °C [53]. <sup>h</sup> pH 7.2 and 22.0 °C [57]. <sup>i</sup> pH 7.2 and 22.0 °C. Ibuprofen was  $1.0 \times 10^{-2} \text{ M}$  [57]. <sup>j</sup> pH 7.0 and 20.0 °C [60]. <sup>k</sup> pH 7.0 and 20.0 °C. Ibuprofen was  $1.0 \times 10^{-2} \text{ M}$  [60]. <sup>l</sup> pH 7.0 and 20.0 °C. Cardiolipin was  $1.6 \times 10^{-4} \text{ M}$  [58]. <sup>m</sup> pH 7.0 and 20.0 °C. Cardiolipin was  $1.6 \times 10^{-4} \text{ M}$  [59]. <sup>n</sup> pH 8.0 and 12.0 °C [56].

scavenging. In particular, the formation of the initial *Mt2/2HbN-ΔpreA-Fe(II)-OONO* species represents the rate limiting step in catalysis, with the conversion of *Mt2/2HbN-ΔpreA-Fe(II)-OONO* to *Mt2/2HbN-ΔpreA-Fe(III)* and  $\text{NO}_3^-/\text{NO}_2^-$  being faster by at least one order of magnitude than the *Mt2/2HbN-ΔpreA-Fe(II)-OONO* complex formation.

The observed rate constant for NO scavenging by *Mt2/2HbN-ΔpreA-Fe(II)-O<sub>2</sub>* (i.e.  $h$ ) increases linearly with the *Mt2/2HbN-ΔpreA-Fe(II)-O<sub>2</sub>* concentration (Fig. 11) according to Eqn (4). The value of the second-order rate constant for NO scavenging by *Mt2/2HbN-ΔpreA-Fe(II)-O<sub>2</sub>* [ $h_{\text{on}} = (2.1 \pm 0.4) \times 10^7 \text{ M}^{-1}\cdot\text{s}^{-1}$ , corresponding to the slope of the linear plot; pH 7.0 and 20.0 °C] is lower by approximately 35-fold than that determined for full-length *Mt2/2HbN-Fe(II)-O<sub>2</sub>* ( $h_{\text{on}} = 7.5 \times 10^8 \text{ M}^{-1}\cdot\text{s}^{-1}$ ; pH 7.5 and 23.0 °C) [11] (Table 3).

Values of  $h_{\text{on}}$  for NO scavenging by ferrous heme proteins range usually between  $6.0 \times 10^5 \text{ M}^{-1}\cdot\text{s}^{-1}$  and  $\geq 6 \times 10^8 \text{ M}^{-1}\cdot\text{s}^{-1}$  (Table 3) [11,63–67; present study]. The very high reactivity of *Mt2/2HbN-Fe(II)-O<sub>2</sub>* ( $7.5 \times 10^8 \text{ M}^{-1}\cdot\text{s}^{-1}$ ) and *Escherichia coli* flavoHb-Fe(II)-O<sub>2</sub> has been postulated to reflect the presence of a Tyr(B10) residue in the heme distal site, together with the high accessibility of NO to the heme-Fe(II)-O<sub>2</sub> center. Based on Resonance Raman studies, it was suggested that the active site structure of *Mt2/2HbN* and *E. coli* flavoHb is tailored to promote O<sub>2</sub>/NO chemistry instead of O<sub>2</sub> delivery, thus explaining their high activity with respect to Mb [30,68]. In particular, in

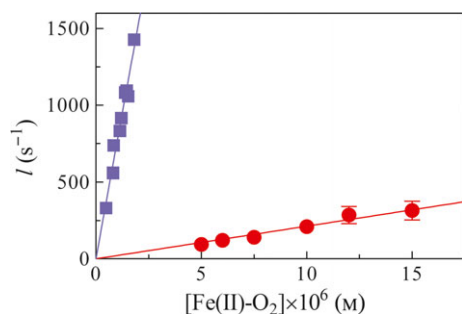


**Fig. 11.** Kinetics of NO scavenging by *Mt2/2HbN-ΔpreA-Fe(II)-O<sub>2</sub>*. Dependence of the pseudo-first-order rate constant for NO scavenging (i.e.  $h$ ) on the *Mt2/2HbN-ΔpreA-Fe(II)-O<sub>2</sub>* (red circles; pH 7.0 and 20.0 °C) and *Mt2/2HbN-Fe(II)-O<sub>2</sub>* (blue squares; pH 7.5 and 23.0 °C) concentration. The continuous lines were calculated according to Eqn (4) (see Materials and methods) with the parameters: *Mt2/2HbN-ΔpreA-Fe(II)-O<sub>2</sub>* –  $h_{\text{on}} = 2.1 \times 10^7 \text{ M}^{-1}\cdot\text{s}^{-1}$ ; and *Mt2/2HbN-Fe(II)-O<sub>2</sub>* –  $h_{\text{on}} = 7.5 \times 10^8 \text{ M}^{-1}\cdot\text{s}^{-1}$ . The NO concentration was  $1.0 \times 10^{-6} \text{ M}$ . Data for NO scavenging by *Mt2/2HbN-Fe(II)-O<sub>2</sub>* were obtained from Ouellet et al. [11]. Where not shown, the SD is smaller than the symbol.

both of these bacterial Hbs, Tyr(B10) interacts with the bound O<sub>2</sub> and may provide a strong electronic pull for activation of the O–O bond, as in peroxidases [30,68]. In line with these observations, it was demonstrated that Tyr(B10) is essential for NO consumption in *2/2HbN* [11,45]. Mutation of Tyr(B10) for Phe in *E. coli* flavoHb reduces the NO-dioxygenase activity by a factor of approximately 30-fold and increases the O<sub>2</sub> dissociation rate constant by 80-fold, highlighting the modulating role of the Tyr(B10) phenoxy group in O<sub>2</sub> binding and NO scavenging [63]. However, other globins displaying the Tyr residue at position B10, such as *M. tuberculosis* 2/2HbO and *Mycobacterium leprae* 2/2HbO, show a much lower reactivity; this behavior was associated with a disfavored accessibility of NO to the heme-Fe(II)-O<sub>2</sub> center [65,67]. Thus, the presence of Tyr(B10) and the efficient diffusion path of ligands to the active site cooperate to accelerate the NO detoxification reaction.

In the absence of the structure of oxygenated ferrous *Mt2/2HbN-ΔpreA*, it is hard to conceive why the pre-A excision results in a 35-fold decrease of the second-order rate constant  $h_{\text{on}}$ . Nevertheless, we may consider that the heme-binding state does not induce significant conformational changes in the distal residues of full-length *Mt2/2HbN-Fe(II)-O<sub>2</sub>* and *Mt2/2HbN-Fe(III)-cyanide* structures (Fig. 2C,D). Furthermore, in the ferric form, the distal sites of *Mt2/2HbN-ΔpreA* and *Mt2/2HbN* match perfectly (Fig. 2C). Therefore, such a good structural match may also be conserved in the oxygenated ferrous forms of full-length and *Mt2/2HbN-ΔpreA*. Thus, the 35-fold decrease of the second-order rate constant  $h_{\text{on}}$  probably results not from specific structural variations at the distal site but, instead, from the hindering of the ligand diffusion path linked to *Mt2/2HbN-ΔpreA* dimerization.

**Table 3.** NO scavenging by ferrous heme proteins.

Heme protein	$h_{\text{on}} (\text{M}^{-1}\cdot\text{s}^{-1})$
<i>M. tuberculosis</i> 2/2-HbN <sup>a</sup>	$7.5 \times 10^8$
<i>M. tuberculosis</i> 2/2HbN-ΔpreA <sup>b</sup>	$2.1 \times 10^7$
<i>M. tuberculosis</i> 2/2-HbO <sup>c</sup>	$6.0 \times 10^5$
<i>M. leprae</i> 2/2-HbO <sup>d</sup>	$2.1 \times 10^6$
<i>E. coli</i> flavoHb <sup>e</sup>	$\geq 6 \times 10^8$
Horse heart Mb <sup>f</sup>	$4.4 \times 10^7$
Murine neuroglobin <sup>g</sup>	$> 7 \times 10^7$
Human Hb <sup>h</sup>	$8.9 \times 10^7$

<sup>a</sup> pH 7.5 and 23.0 °C [11]. <sup>b</sup> pH 7.0 and 20.0 °C. Present study. <sup>c</sup> pH 7.5 and 23.0 °C [65]. <sup>d</sup> pH 7.3 and 20.0 °C [67]. <sup>e</sup> pH 7.0 and 20.0 °C [63]. <sup>f</sup> pH 7.0 and 20.0 °C [64]. <sup>g</sup> pH 7.0 and 20.0 °C [66]. <sup>h</sup> pH 7.0 and 20.0 °C [64].

## Discussion

*M. tuberculosis* exhibits resistance mechanisms that help the bacterium to evade the toxic effects of NO and nitrosative stress. One of the unique defense mechanisms by which it can protect itself from reactive nitrogen species relies on the oxygenated form of group I *Mt2/2HbN*, a monomeric protein displaying potent O<sub>2</sub>-dependent NOD activity [10,11,23,24]. X-ray crystallographic and computational studies have highlighted the relationship between the protein structure and the NOD activity of key residues in *Mt2/2HbN*. In particular, the NO detoxification activity of *Mt2/2HbN* largely depends on the efficiency of ligand migration to the heme cavity, a process that has been proposed to follow a distinct dual path for the diffusion of O<sub>2</sub> and NO to the heme through a two-branched protein matrix tunnel system [26,34]. MD simulations on the full-length protein indicated that O<sub>2</sub> diffusion towards the distal site would occur through long and short branches of the tunnel system. O<sub>2</sub>-binding to the heme-Fe would trigger a ligand-induced conformational change(s) regulating/facilitating the opening of the long tunnel branch via Phe(62)E15, which would act as a gate for NO entry [27,45]. According to a different MD simulation approach, the short tunnel branch would also act as a diffusion path for NO entrance [41].

Recently, the NOD activity of *Mt2/2HbN* has been correlated with the presence of a short pre-A region at its N-terminus, which is not conserved in most 2/2HbNs [7,29]. Strikingly, the deletion of the pre-A region in *Mt2/2HbN* drastically reduces its ability to scavenge NO (present study), whereas the insertion of the pre-A region at the N-terminus of *M. smegmatis* 2/2HbN (lacking the pre-A region) improved the protein NOD activity [29]. Extended MD simulations carried out on the oxygenated monomeric *Mt2/2HbN* showed that the excision of the pre-A region results in distinct changes in the protein dynamics (particularly of the B- and E-helices) relative to full-length *Mt2/2HbN*. Such changes result in the Phe(62)E15 gate of the long tunnel branch being trapped in a conformation that substantially impedes migration of NO toward the heme distal site, thus hampering the efficient NO-detoxification ability of the protein [29].

The crystal structure of *Mt2/2HbN-ΔpreA* unexpectedly reveals that removal of the pre-A region results in long range effects on the C-terminal backbone conformation, promoting the assembly of a stable dimer, where access of heme ligands through the short tunnel branch (whose entry site falls at the dimerization interface) is hindered. Indeed, MD simulations on the deoxygenated *Mt2/2HbN-ΔpreA* dimer show that the

long tunnel branch is the only accessible pathway for O<sub>2</sub>-ligand migration to the heme, both from and to the solvent. The *Mt2/2HbN-ΔpreA* dimeric crystal structure also shows that the phenyl ring of the gating residue Phe(62)E15 partly restricts the diameter of the tunnel. This is in agreement with the results obtained from MD simulations, which reveal that the open/closed transitions of the gating residues occur in both subunits of the dimer (both oxygenated and deoxygenated). However, diffusion of the ligand through the long tunnel branch pathway is less efficient in *Mt2/2HbN-ΔpreA* relative to the full-length protein, possibly as a result of a slight restriction of the tunnel at the Phe(62)E15 site, resulting from the closer positioning of the E- and H-helices in the dimer. Indeed, the  $k_{\text{on}}$  value for peroxyxynitrite isomerization by *Mt2/2HbN-ΔpreA-Fe(III)* is only four-fold lower than that reported for the full-length protein, and the kinetics of NO scavenging by *Mt2/2HbN-ΔpreA-Fe(II)-O<sub>2</sub>* is reduced by 35-fold relative to that catalyzed by full-length *Mt2/2HbN*.

Overall, our data suggest that deletion of the pre-A region significantly reduces the ability of *Mt2/2HbN* to scavenge NO, first by interfering with the ligand diffusion mechanism that supplies O<sub>2</sub> and NO to the heme-distal site in the full-length protein. In *Mt2/2HbN-ΔpreA*, the long tunnel branch is the main/only diffusion path available for gaseous diatomic ligands, rendering the NOD activity significantly less efficient, as also a result of the diffusion of ligands within the protein partly being restricted at the Phe(62)E15 residue. Furthermore, MD simulations suggest that the *Mt2/2HbN-ΔpreA* monomer exhibits a drastic change in the dynamical behavior of the protein backbone, which reduces the relative motion of B and E helices, hampering the conformational transitions between the open and closed states of the gating Phe(62)E15 residue [29].

On the basis of the results reported in the present study, it might be speculated that *Mt2/2HbN* evolved to host the pre-A region as a mechanism reinforcing the survival of the microorganism against the reactive nitrosative stress in macrophages. In this respect, it is worth noting that recent studies have highlighted the presence of *Mt2/2HbN* among the lipophilic proteins associated with the cell membrane and the cell wall [69,70]. Notably, NMR data and MD simulations have indicated that membrane association occurs via the pre-A region and the G- and H-helices [71]. Modeling indicates that, in the *Mt2/2HbN* membrane-bound form, the short tunnel branch would be oriented toward the membrane interior, thus favoring the uptake of nonpolar substrates from the membrane. In

this context, the presence of the pre-A region could be viewed as an evolutionary adaptation preventing *Mt2/2HbN* dimerization in the cell, as well as facilitating the association with the membrane and the uptake of gaseous ligands (most likely NO) through the short tunnel branch, thus contributing to the achievement of efficient NO-dioxygenase activity.

## Materials and methods

### Crystallization, structure determination and refinement

*Mt2/2HbN-ΔpreA*, lacking the pre-A region (residues 1–11), was expressed and purified as described previously [42]. Crystals of ferric *Mt2/2HbN-ΔpreA* were grown at 4 °C by vapor diffusion methods under the growth conditions: 2.0 M Na-formate and 0.1 M Na-acetate, pH 4.6 (Crystal Screen I, condition 34; Hampton Research, Aliso Viejo, CA, USA). Crystals were cryoprotected in their mother liquor (3.0 M Na-formate, 0.1 M Na-acetate, pH 4.6) supplemented with 15% (v/v) glycerol and flash-frozen in liquid nitrogen. A single crystal, belonging to the hexagonal *P*<sub>6</sub>,22 space group (one protein molecule in the asymmetric unit) diffracted at a resolution of 1.53 Å, using synchrotron radiation (beamline ID23-1; ESRF, Grenoble, France). Raw data were processed with MOSFLM [72] and SCALA [73].

The structure was solved by molecular replacement methods with PHASER [74], using the *Mt2/2HbN* structure (PDB code: [1IDR](#)) as the search model, from which the first 11 N-terminal residues had been deleted. Model building/inspection and restrained refinement were performed with COOT [75] and REFMAC [76], respectively. Data collection and refinement statistics are reported in Table 1. MOLPROBITY [77] and SURFNET [78] were used to assess stereochemical quality, and to explore protein matrix cavities. PISA ([http://www.ebi.ac.uk/msd-srv/prot\\_int/cgi-bin/piserver](http://www.ebi.ac.uk/msd-srv/prot_int/cgi-bin/piserver)) [49] was used to identify protein quaternary assembly.

### DLS

The *Mt2/2HbN-ΔpreA* protein solution (1.0 mg·mL<sup>-1</sup> in 50 mM Tris-HCl buffer, pH 7.5) was centrifuged at 13 000 *g* for 10 min prior to DLS analysis. DLS data were acquired at 10 °C, 20 scans, 30 s for each scan, using a Protein Solutions DynaPro 99 instrument with a DynaProMSTC200 microsampler (Protein Solutions, Charlottesville, VA, USA). Data analysis was performed using DYNAMICS, version 6 (Protein Solutions).

### MD simulations

MD simulations were performed to examine the intrinsic dynamics of the protein. Calculations were performed with

the PMEMD.cuda module of the AMBER12 suite [79]. The parm99SB force field [80] was used for the protein, and the heme parameters were taken from previous studies [81,82]. The protein was immersed in a pre-equilibrated octahedral box of TIP3P water molecules [83] and counter-ions were added to maintain the neutrality of the simulated system, which contained the protein (dimer), 16 Na<sup>+</sup> cations and approximately 10 000 water molecules. Thermalization and equilibration were accomplished by a multistep protocol, involving an optimization of the initial structures, and then slow heating to the target temperature (298 K) in a 2 ns MD at constant volume, followed by 2 ns MD at constant pressure (1 bar). Next, productive simulations were performed in the NPT ensemble using periodic boundary conditions, the SHAKE algorithm [84] to constrain the bonds connecting hydrogen and heavy atoms, and a 1 fs time step for the integration of Newton's equations. Furthermore, a Langevin collision frequency of 2 ps<sup>-1</sup> [85], particle mesh Ewald for electrostatic interactions [86] and a cut-off of 10 Å for non-covalent interactions were also used. Frames were collected at 10 ps intervals for subsequent analysis of the trajectories.

### Analysis of the ligand migration pathways

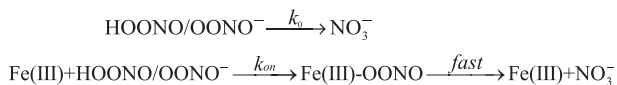
ILS calculations were used to examine the O<sub>2</sub> migration inside the protein matrix [87]. ILS has been widely used to examine the migration of gaseous ligands in proteins, and the results have shown that this method is well suited for disclosing the topological features of tunnels [88–90]. Furthermore, the energetics profile for the ligand migration is also provided by ILS, as long as this method relies on a Boltzmann-weighted average of the interaction energy between the ligand and an ensemble of protein snapshots. Calculations were performed using an O<sub>2</sub> molecule as probe ligand and a set of 5000 frames taken from the last 90 ns of simulation time, which were aligned and enclosed in a rectangular grid (resolution of 0.5 Å). The values for grid size, resolution and frame numbers were tested thoroughly in a previous study [87]. Analysis of the ILS data was performed using inhouse software (available upon request).

### Kinetics of peroxynitrite isomerization by *Mt2/2HbN-ΔpreA-Fe(III)*

Peroxynitrite was obtained from Caiman Chemical Company (Ann Arbor, MI, USA) and stored in small aliquots at -80.0 °C. The concentration of peroxynitrite was determined spectrophotometrically by measuring *A*<sub>302</sub>. The peroxynitrite stock solution (2.0 × 10<sup>-3</sup> M) was diluted immediately before use with degassed 1.0 × 10<sup>-2</sup> M NaOH to reach the desired concentration [51].

Kinetics of peroxynitrite isomerization in the presence of *Mt2/2HbN-ΔpreA-Fe(III)* was recorded at 302 nm by rapidly mixing the *Mt2/2HbN-ΔpreA-Fe(III)* solution (final

concentration  $2.0 \times 10^{-6}$  M to  $1.0 \times 10^{-5}$  M;  $1.0 \times 10^{-1}$  M phosphate buffer, pH 7.0; 20.0 °C) with the peroxy-nitrite solution (final concentration  $5.0 \times 10^{-5}$  M) [52–54, 57] and analyzed in the framework of the minimum reaction mechanism depicted by Scheme 1 [51]:



**Scheme 1.** Peroxynitrite isomerization mechanism

Values of the pseudo first-order rate constant for peroxy-nitrite isomerisation in the presence of *Mt2/2HbN-ΔpreA-Fe(III)* (i.e.  $k$ ) were determined from the analysis of the time-dependent decrease in  $A_{302}$ , according to Eqn (1) [51]:

$$[\text{HOONO/OONO}^-]_t = [\text{HOONO/OONO}^-]_i \times e^{-k \times t} \quad (1)$$

Values of the second-order rate constant for *Mt2/2HbN-ΔpreA-Fe(III)*-mediated peroxy-nitrite isomerization (i.e.  $k_{\text{on}}$ ) and of the first-order rate constant for peroxy-nitrite isomerization in the absence of *Mt2/2HbN-ΔpreA-Fe(III)* (i.e.  $k_0$ ) were determined according to Eqn (2) [51]:

$$k = k_{\text{on}} \times [\text{Mt2/2HbN-}\Delta\text{preA-Fe(III)}] + k_0 \quad (2)$$

**Kinetics of NO scavenging by *Mt2/2HbN-ΔpreA-Fe(II)-O<sub>2</sub>***

For preparation of *Mt2/2HbN-ΔpreA-Fe(II)-O<sub>2</sub>*, a few grains of sodium dithionite were added to the *Mt2/2HbN-ΔpreA-Fe(III)* solution. Then, the unreacted dithionite and the reaction products were separated from the *Mt2/2HbN-ΔpreA-Fe(II)* sample by passing the *Mt2/2HbN-ΔpreA-Fe(II)* solution through a Sephadex G10 column (GE Healthcare, Little Chalfont, UK) under aerobic conditions. This procedure led to *Mt2/2HbN-ΔpreA-Fe(II)* oxygenation [91]. NO (Sigma-Aldrich, Milwaukee, WI, USA) was purified by flowing it through a NaOH column to remove acidic nitrogen oxides. The NO solution was prepared by keeping the  $1.0 \times 10^{-1}$  M phosphate buffer solution (pH 7.0) in a closed vessel under NO at 760 mmHg anaerobically (20.0 °C) [11].

Kinetics of NO scavenging by *Mt2/2HbN-ΔpreA-Fe(II)-O<sub>2</sub>* was recorded at 416 nm by rapidly mixing the *Mt2/2HbN-ΔpreA-Fe(II)-O<sub>2</sub>* solution (final concentration  $5.0 \times 10^{-6}$  M to  $1.5 \times 10^{-5}$  M;  $1.0 \times 10^{-1}$  M phosphate buffer, pH 7.0; 20.0 °C) with the NO solution (final concentration of approximately  $1 \times 10^{-6}$  M) [11] and analyzed in the framework of the minimum reaction mechanism depicted by Scheme 2:



**Scheme 2.** NO scavenging mechanism

Values of the pseudo first-order rate constant for NO scavenging by *Mt2/2HbN-ΔpreA-Fe(II)-O<sub>2</sub>* (i.e.  $h$ ) were determined according to Eqn (3) [11]:

$$[\text{Fe(II)} - \text{O}_2]_t = [\text{Fe(II)-O}_2]_i \times e^{-h \times t} \quad (3)$$

The value of the second-order rate constant for NO scavenging by *Mt2/2HbN-ΔpreA-Fe(II)-O<sub>2</sub>* (i.e.  $h_{\text{on}}$ ) was determined according to Eqn (4) [11]:

$$h = h_{\text{on}} \times [\text{Mt2/2HbN-}\Delta\text{preA-Fe(II)-O}_2] \quad (4)$$

**Acknowledgements**

This work was supported by grant CAL 2015 of Roma Tre University to PA, and by funds from the Spanish Ministerio de Economía y Competitividad (SAF2014-57094-R) and the Generalitat de Catalunya (2014-SGR-1189) to FJL. FJL also thanks the ICREA Academia Foundation for financial support. The Barcelona Supercomputer Center is acknowledged for providing access to supercomputational resources.

**Author contributions**

AS and MG performed the expression and purification experiments. AP and MN crystallized the protein, measured and processed diffraction data, and refined the crystal structure. JPB, AB-C, LB, DAE and FJL performed the MD simulations. PA performed the kinetics experiments. MB, PA, DAE, FJL and MN planned the experiments. All authors contributed to the writing of the paper.

**References**

- 1 Wittenberg JB, Bolognesi M, Wittenberg BA & Guertin M (2002) Truncated hemoglobins: a new family of hemoglobins widely distributed in bacteria, unicellular eukaryotes, and plants. *J Biol Chem* **277**, 871–874.
- 2 Vuletich DA & Lecomte JT (2006) A phylogenetic and structural analysis of truncated hemoglobins. *J Mol Evol* **62**, 196–210.
- 3 Nardini M, Pesce A, Milani M & Bolognesi M (2007) Protein fold and structure in the truncated (2/2) globin family. *Gene* **398**, 2–11.
- 4 Vinogradov SN, Tinajero-Trejo M, Poole RK & Hoogewijs D (2013) Bacterial and archaeal globins – a revised perspective. *Biochim Biophys Acta* **1834**, 1789–1800.
- 5 Perutz MF (1979) Regulation of oxygen affinity of hemoglobin: influence of structure of the globin on the heme iron. *Annu Rev Biochem* **48**, 327–386.

- 6 Pesce A, Couture M, Dewilde S, Guertin M, Yamauchi K, Ascenzi P, Moens L & Bolognesi M (2000) A novel two-over-two alpha-helical sandwich fold is characteristic of the truncated hemoglobin family. *EMBO J* **19**, 2424–2434.
- 7 Pesce A, Bolognesi M & Nardini M (2013) The diversity of 2/2 (truncated) globins. *Adv Microb Physiol* **63**, 49–78.
- 8 Milani M, Savard PY, Ouellet H, Ascenzi P, Guertin M & Bolognesi M (2003) A TyrCD1/TrpG8 hydrogen bond network and a TyrB10/TyrCD1 covalent link shape the heme distal site of *Mycobacterium tuberculosis* hemoglobin O. *Proc Natl Acad Sci USA* **100**, 5766–5771.
- 9 Nardini M, Pesce A, Labarre M, Richard C, Bolli A, Ascenzi P, Guertin M & Bolognesi M (2006) Structural determinants in the group III truncated hemoglobin from *Campylobacter jejuni*. *J Biol Chem* **281**, 37803–37812.
- 10 Couture M, Yeh SR, Wittenberg BA, Wittenberg JB, Ouellet Y, Rousseau DL & Guertin M (1999) A cooperative oxygen-binding hemoglobin from *Mycobacterium tuberculosis*. *Proc Natl Acad Sci USA* **96**, 11223–11228.
- 11 Ouellet H, Ouellet Y, Richard C, Labarre M, Wittenberg B, Wittenberg J & Guertin M (2002) Truncated hemoglobin HbN protects *Mycobacterium bovis* from nitric oxide. *Proc Natl Acad Sci USA* **99**, 5902–5907.
- 12 Vinogradov SN & Moens L (2008) Diversity of globin function: enzymatic, transport, storage, and sensing. *J Biol Chem* **283**, 8773–8777.
- 13 Nicoletti FP, Comandini A, Bonamore A, Boechi L, Boubeta FM, Feis A, Smulevich G & Boffi A (2010) Sulfide binding properties of truncated hemoglobins. *Biochemistry* **49**, 2269–2278.
- 14 Parrilli E, Giuliani M, Giordano D, Russo R, Marino G, Verde C & Tutino ML (2010) The role of a 2-on-2 haemoglobin in oxidative and nitrosative stress resistance of Antarctic *Pseudoalteromonas haloplanktis* TAC125. *Biochimie* **92**, 1003–1009.
- 15 Scott NL, Xu Y, Shen G, Vuletich DA, Falzone CJ, Li Z, Ludwig M, Pond MP, Preimesberger MR, Bryant DA *et al.* (2010) Functional and structural characterization of the 2/2 hemoglobin from *Synechococcus* sp. PCC 7002. *Biochemistry* **49**, 7000–7011.
- 16 Vinogradov SN, Hoogewijs D, Bailly X, Arredondo-Peter R, Gough J, Dewilde S, Moens L & Vanfleteren JR (2006) A phylogenomic profile of globins. *BMC Evol Biol* **6**, 31–47.
- 17 MacMicking JD, North RJ, LaCourse R, Mudgett JS, Shah SK & Nathan CF (1997) Identification of nitric oxide synthase as a protective locus against tuberculosis. *Proc Natl Acad Sci USA* **94**, 5243–5248.
- 18 Nathan C & Shiloh MU (2000) Reactive oxygen and nitrogen intermediates in the relationship between mammalian hosts and microbial pathogens. *Proc Natl Acad Sci USA* **97**, 8841–8848.
- 19 Cooper AM, Adams LB, Dalton DK, Appelberg R & Ehlers S (2002) IFN-gamma and NO in mycobacterial disease: new jobs for old hands. *Trends Microbiol* **10**, 221–226.
- 20 Visca P, Fabozzi G, Milani M, Bolognesi M & Ascenzi P (2002) Nitric oxide and *Mycobacterium leprae* pathogenicity. *IUBMB Life* **54**, 95–99.
- 21 Ohno H, Zhu G, Mohan VP, Chu D, Kohno S, Jacobs WR Jr & Chan J (2003) The effects of reactive nitrogen intermediates on gene expression in *Mycobacterium tuberculosis*. *Cell Microbiol* **5**, 637–648.
- 22 Schnappinger D, Schoolnik GK & Ehrt S (2006) Expression profiling of host pathogen interactions: how *Mycobacterium tuberculosis* and the macrophage adapt to one another. *Microbes Infect* **8**, 1132–1140.
- 23 Pathania R, Navani NK, Gardner AM, Gardner PR & Dikshit KL (2002) Nitric oxide scavenging and detoxification by the *Mycobacterium tuberculosis* haemoglobin HbN in *Escherichia coli*. *Mol Microbiol* **45**, 1303–1314.
- 24 Pawaria S, Rajamohan G, Gambhir V, Lama A, Varshney GC & Dikshit KL (2007) Intracellular growth and survival of *Salmonella enterica* serovar *Typhimurium* carrying truncated hemoglobins of *Mycobacterium tuberculosis*. *Microb Pathog* **42**, 119–128.
- 25 Gardner PR (2012) Hemoglobin: a nitric-oxide dioxygenase. *Scientifica* ID 683729.
- 26 Milani M, Pesce A, Ouellet Y, Ascenzi P, Guertin M & Bolognesi M (2001) *Mycobacterium tuberculosis* hemoglobin N displays a protein tunnel suited for O<sub>2</sub> diffusion to the heme. *EMBO J* **20**, 3902–3909.
- 27 Bidon-Chanal A, Crespo A, Milani M, Orozco M, Bolognesi M, Luque FJ & Estrin DA (2006) Ligand-induced dynamical regulation of NO conversion in *Mycobacterium tuberculosis* truncated hemoglobin-N. *Proteins* **64**, 457–464.
- 28 Daigle R, Guertin M & Lagüe P (2009) Structural characterization of the tunnels of *Mycobacterium tuberculosis* truncated haemoglobin N from molecular dynamics simulations. *Proteins* **75**, 735–747.
- 29 Lama A, Pawaria S, Bidon-Chanal A, Anand A, Gelpí JL, Arya S, Martí M, Estrin DA, Luque FJ & Dikshit KL (2009) Role of Pre-A motif in nitric oxide scavenging by truncated hemoglobin, HbN, of *Mycobacterium tuberculosis*. *J Biol Chem* **284**, 14457–14468.
- 30 Yeh SR, Couture M, Ouellet Y, Guertin M & Rousseau DL (2000) A cooperative oxygen binding hemoglobin from *Mycobacterium tuberculosis*.

- Stabilization of heme ligands by a distal tyrosine residue. *J Biol Chem* **275**, 1679–1684.
- 31 Milani M, Ouellet Y, Ouellet H, Guertin M, Boffi A, Antonini G, Bocedi A, Mattu M, Bolognesi M & Ascenzi P (2004) Cyanide binding to truncated hemoglobins: a crystallographic and kinetic study. *Biochemistry* **43**, 5213–5221.
- 32 Ouellet Y, Milani M, Couture M, Bolognesi M & Guertin M (2006) Ligand interactions in the distal heme pocket of *Mycobacterium tuberculosis* truncated hemoglobin N: roles of TyrB10 and GlnE11 residues. *Biochemistry* **45**, 8770–8781.
- 33 Ouellet YH, Daigle R, Lagüe P, Dantsker D, Milani M, Bolognesi M, Friedman JM & Guertin M (2008) Ligand binding to truncated hemoglobin N from *Mycobacterium tuberculosis* is strongly modulated by the interplay between the distal heme pocket residues and internal water. *J Biol Chem* **283**, 27270–27278.
- 34 Milani M, Pesce A, Ouellet Y, Dewilde S, Friedman J, Ascenzi P, Guertin M & Bolognesi M (2004) Heme-ligand tunneling in group I truncated hemoglobins. *J Biol Chem* **279**, 21520–21525.
- 35 Pesce A, Milani M, Nardini M & Bolognesi M (2008) Mapping heme-ligand tunnels in group I truncated(2/2) hemoglobins. *Methods Enzymol* **436**, 303–315.
- 36 Saam J, Rosini E, Molla G, Schulten K, Pollegioni L & Ghisla S (2010) O<sub>2</sub>-reactivity of flavoproteins: dynamic access of dioxygen to the active site and role of a H<sup>+</sup> relay system in d-amino acid oxidase. *J Biol Chem* **285**, 24439–24446.
- 37 Oliveira AS, Damas JM, Baptista AM & Soares CM (2014) Exploring O<sub>2</sub> diffusion in A-type cytochrome *c* oxidases: molecular dynamics simulations uncover two alternative channels towards the binuclear site. *PLoS Comput Biol* **10**, e1004010.
- 38 Wang P-H, Best RB & Blumberg J (2011) Multiscale simulation reveals multiple pathways for H<sub>2</sub> and O<sub>2</sub> transport in a [NiFe]-hydrogenase. *J Am Chem Soc* **133**, 3548–3556.
- 39 Brunori M & Gibson QH (2001) Cavities and packing defects in the structural dynamics of myoglobin. *EMBO Rep* **2**, 674–679.
- 40 Regmi CK, Bhandari YR, Gerstman BS & Chapagain PP (2013) Exploring the diffusion of molecular oxygen in the red fluorescent protein mCherry using explicit oxygen molecular dynamics simulations. *J Phys Chem B* **117**, 2247–2253.
- 41 Daigle R, Rousseau JA, Guertin M & Lagüe P (2009) Theoretical investigations of nitric oxide channeling in *Mycobacterium tuberculosis* truncated hemoglobin N. *Biophys J* **97**, 2967–2977.
- 42 Savard P-Y, Daigle R, Morin S, Sebilo A, Meindre F, Lagüe P, Guertin M & Gagné SM (2011) Structure and dynamics of *Mycobacterium tuberculosis* truncated hemoglobin N: insights from NMR spectroscopy and molecular dynamics simulations. *Biochemistry* **50**, 11121–11130.
- 43 Boron I, Bustamante JP, Davidge KS, Singh S, Forti F, Bowman LAH, Tinajero-Trejo M, Poole R, Dikshit K, Estrin DA *et al.* (2015) Ligand uptake by *M. tuberculosis* truncated hemoglobin N is modulated by both two tunnels and retained water molecules. *F1000Res* **4**, 22.
- 44 Crespo A, Martí MA, Kalko SG, Morreale A, Orozco M, Gelpi JL, Luque FJ & Estrin DA (2005) Theoretical study of the truncated hemoglobin HbN: exploring the molecular basis of the NO detoxification mechanism. *J Am Chem Soc* **127**, 4433–4444.
- 45 Bidon-Chanal A, Martí MA, Estrin DA & Luque FJ (2007) Dynamical regulation of ligand migration by a gate-opening molecular switch in truncated hemoglobin-N from *Mycobacterium tuberculosis*. *J Am Chem Soc* **129**, 6782–6788.
- 46 Mishra S & Meuwly M (2009) Nitric oxide dynamics in truncated hemoglobin: docking sites, migration pathways, and vibrational spectroscopy from molecular dynamics simulations. *Biophys J* **96**, 2105–2118.
- 47 Oliveira A, Singh S, Bidon-Chanal A, Forti F, Martí MA, Boechi L, Estrin DA, Dikshit KL & Luque FJ (2012) Role of PheE15 gate in ligand entry and nitric oxide detoxification function of *Mycobacterium tuberculosis* truncated hemoglobin N. *PLoS One* **7**, e49291.
- 48 Singh S, Thakur N, Oliveira A, Petruk AA, Hade MD, Sethi D, Bidon-Chanal A, Martí MA, Datta H, Parkesh R *et al.* (2014) Mechanistic insight into the enzymatic reduction of truncated hemoglobin N of *Mycobacterium tuberculosis*: role of the CD loop and pre-A motif in electron cycling. *J Biol Chem* **289**, 21573–21583.
- 49 Krissinel E & Henrick K (2005) Detection of protein assemblies in crystals. In *Computational Life Science* (Berthold MR *et al.*, eds). pp. 163–174. CompLife Springer-Verlag, Berlin, Heidelberg.
- 50 Reeder BJ & Hough MA (2014) The structure of a class 3 nonsymbiotic plant haemoglobin from *Arabidopsis thaliana* reveals a novel N-terminal helical extension. *Acta Crystallogr D* **70**, 1411–1418.
- 51 Ascenzi P, Coletta A, Cao Y, Trezza V, Leboffe L, Fanali G, Fasano M, Pesce A, Ciaccio C, Marini S *et al.* (2013) Isoniazid inhibits the heme-based reactivity of *Mycobacterium tuberculosis* truncated hemoglobin N. *PLoS One* **8**, e69762.
- 52 Pfeiffer S, Gorren AC, Schmidt K, Werner ER, Hansert B, Bohle DS & Mayer B (1997) Metabolic fate of peroxynitrite in aqueous solution: reaction with nitric oxide and pH-dependent decomposition to nitrite and oxygen in a 2:1 stoichiometry. *J Biol Chem* **272**, 3465–3470.

- 53 Herold S & Kalinga S (2003) Metmyoglobin and methemoglobin catalyze the isomerization of peroxyxynitrite to nitrate. *Biochemistry* **42**, 14036–14046.
- 54 Herold S, Kalinga S, Matsui T & Watanabe Y (2004) Mechanistic studies of the isomerization of peroxyxynitrite to nitrate catalyzed by distal histidine metmyoglobin mutants. *J Am Chem Soc* **126**, 6945–6955.
- 55 Goldstein S, Lind J & Merényi G (2005) Chemistry of peroxyxynitrites as compared to peroxyxynitrates. *Chem Rev* **105**, 2457–2470.
- 56 Mehl M, Daiber A, Herold S, Shoun H & Ullrich V (1999) Peroxyxynitrite reaction with heme proteins. *Nitric Oxide* **3**, 142–152.
- 57 Ascenzi P, di Masi A, Coletta M, Ciaccio C, Fanali G, Nicoletti FP, Smulevich G & Fasano M (2009) Ibuprofen impairs allosterically peroxyxynitrite isomerization by ferric human serum heme-albumin. *J Biol Chem* **284**, 31006–31017.
- 58 Ascenzi P, Ciaccio C, Sinibaldi F, Santucci R & Coletta M (2011) Cardiolipin modulates allosterically peroxyxynitrite detoxification by horse heart cytochrome *c*. *Biochem Biophys Res Commun* **404**, 190–194.
- 59 Ascenzi P, Ciaccio C, Sinibaldi F, Santucci R & Coletta M (2011) Peroxyxynitrite detoxification by horse heart carboxymethylated cytochrome *c* is allosterically modulated by cardiolipin. *Biochem Biophys Res Commun* **415**, 463–467.
- 60 di Masi A, Gullotta F, Bolli A, Fanali G, Fasano M & Ascenzi P (2011) Ibuprofen binding to secondary sites allosterically modulates the spectroscopic and catalytic properties of human serum heme-albumin. *FEBS J* **278**, 654–662.
- 61 Coppola D, Giordano D, Tinajero-Trejo M, di Prisco G, Ascenzi P, Poole RK & Verde C (2013) Antarctic bacterial hemeoglobin and its role in the protection against nitrogen reactive species. *Biochim Biophys Acta* **1834**, 1923–1931.
- 62 Ascenzi P, Leboffe L, Pesce A, Ciaccio C, Sbardella D, Bolognesi M & Coletta M (2014) Nitrite-reductase and peroxyxynitrite isomerization activities of *Methanosarcina acetivorans* protoglobin. *PLoS One* **9**, e95391.
- 63 Gardner AM, Martin LA, Gardner PR, Dou Y & Olson JS (2000) Steady-state and transient kinetics of *Escherichia coli* nitric-oxide dioxygenase (flavoheemoglobin). The B10 tyrosine hydroxyl is essential for dioxygen binding and catalysis. *J Biol Chem* **275**, 12581–12589.
- 64 Herold S, Exner M & Nauser T (2001) Kinetic and mechanistic studies of the NO<sup>•</sup>-mediated oxidation of oxyheemoglobin and oxyheemoglobin. *Biochemistry* **40**, 3385–3395.
- 65 Ouellet H, Juszczak L, Dantsker D, Samuni U, Ouellet YH, Savard PY, Wittenberg JB, Wittenberg BA, Friedman JM & Guertin M (2003) Reactions of *Mycobacterium tuberculosis* truncated hemoglobin O with ligands reveal a novel ligand-inclusive hydrogen bond network. *Biochemistry* **42**, 5764–5774.
- 66 Brunori M, Giuffrè A, Nienhaus K, Nienhaus GU, Scandurra FM & Vallone B (2005) Neuroglobin, nitric oxide, and oxygen: functional pathways and conformational changes. *Proc Natl Acad Sci USA* **102**, 8483–8488.
- 67 Ascenzi P, Bocedi A, Bolognesi M, Fabozzi G, Milani M & Visca P (2006) Nitric oxide scavenging by *Mycobacterium leprae* G1bO involves the formation of the ferric heme-bound peroxyxynitrite intermediate. *Biochem Biophys Res Commun* **339**, 448–454.
- 68 Mukai M, Mills CE, Poole RK & Yeh SR (2001) Flavoheemoglobin, a globin with a peroxidase-like catalytic site. *J Biol Chem* **276**, 7272–7277.
- 69 Målen H, Pathak S, Sjøteland T, de Souza GA & Wiker HG (2010) Definition of novel cell envelope associated proteins in Triton X-114 extracts of *Mycobacterium tuberculosis* H37Rv. *BMC Microbiol* **10**, 132–143.
- 70 Arya S, Sethi D, Singh S, Hade MD, Singh V, Raju P, Chodiseti SB, Verma D, Varshney GC, Agrewala JN *et al.* (2013) Truncated hemoglobin, HbN, is post-translationally modified in *Mycobacterium tuberculosis* and modulates host-pathogen interactions during intracellular infection. *J Biol Chem* **288**, 29987–29999.
- 71 Rhéault J-F, Gagné È, Guertin M, Lamoureux G, Auger M & Lagüe P (2015) Molecular model of hemoglobin N from *Mycobacterium tuberculosis* bound to lipid bilayers: a combined spectroscopic and computational study. *Biochemistry* **54**, 2073–2084.
- 72 Leslie AGM (2003) MOSFLM User Guide, Mosflm Version 6.2.3. MRC Laboratory of Molecular Biology, Cambridge, UK.
- 73 Evans P (2006) Scaling and assessment of data quality. *Acta Crystallogr D* **62**, 72–82.
- 74 Storoni LC, McCoy AJ & Read RJ (2004) Likelihood-enhanced fast rotation functions. *Acta Crystallogr D* **60**, 432–438.
- 75 Emsley P & Cowtan K (2004) Coot: model-building tools for molecular graphics. *Acta Crystallogr D* **60**, 2126–2132.
- 76 Murshudov GN, Vagin AA & Dodson EJ (1997) Refinement of macromolecular structures by the maximum-likelihood method. *Acta Crystallogr D* **53**, 240–255.
- 77 Chen VB, Arendall WB III, Headd JJ, Keedy DA, Immormino RM, Kapral GJ, Murray LW, Richardson JS & Richardson DC (2010) MolProbity: all-atom structure validation for macromolecular crystallography. *Acta Crystallogr D* **66**, 12–21.
- 78 Laskowski RA (1995) SURFNET: a program for visualizing molecular surfaces, cavities and

- intermolecular interactions. *J Mol Graph* **13**, 323–330.
- 79 Case DA, Darden TA, Cheatham TE III, Simmerling CL, Wang J, Duke RE, Luo R, Walker RC, Zhang W, Merz KM *et al.* (2012) AMBER 12. University of California, San Francisco.
- 80 Hornak V, Abel R, Okur A, Strockbine B, Roitberg A & Simmerling C (2006) Comparison of multiple Amber force fields and development of improved protein backbone parameters. *Proteins* **65**, 712–725.
- 81 Capece L, Boechi L, Perissinotti LL, Arroyo-Mañez P, Bikiel DE, Smulevich G, Martí MA & Estrin DA (2013) Small ligand-globin interactions: reviewing lessons derived from computer simulation. *Biochim Biophys Acta* **1834**, 1722–1738.
- 82 Martí MA, Capece L, Bidon-Chanal A, Crespo A, Guallar V, Luque FJ & Estrin DA (2008) NO reactivity with globins as investigated through computer simulation. *Methods Enzymol* **437**, 477–498.
- 83 Jorgensen WL, Chandrasekhar J, Madura JD, Impey RW & Klein ML (1983) Comparison of simple potential functions for simulating liquid water. *J Chem Phys* **79**, 926–935.
- 84 Ryckaert J-P, Ciccotti G & Berendsen HJC (1977) Numerical integration of the cartesian equations of motion of a system with constraints: molecular dynamics of n-alkanes. *J Comput Phys* **23**, 327–341.
- 85 Wu X & Brooks BR (2003) Self-guided Langevin dynamics simulation method. *Chem Phys Lett* **381**, 512–518.
- 86 Darden T, York D & Pedersen L (1993) Particle mesh Ewald: an N-log(N) method for Ewald sums in large systems. *J Chem Phys* **98**, 10089–10092.
- 87 Cohen J, Olsen KW & Schulten K (2008) Finding gas migration pathways in proteins using implicit ligand sampling. *Methods Enzymol* **437**, 439–457.
- 88 Forti F, Boechi L, Estrin DA & Martí MA (2011) Comparing and combining implicit ligand sampling with multiple steered molecular dynamics to study ligand migration processes in heme proteins. *J Comp Chem* **32**, 2219–2231.
- 89 Arroyo-Mañez P, Bikiel DE, Boechi L, Capece L, Di Lella S, Estrin DA, Martí MA, Moreno DM, Nadra AD & Petruk AA (2011) Protein dynamics and ligand migration as studied by computer simulation. *Biochim Biophys Acta* **1814**, 1054–1064.
- 90 Abbruzzetti S, Spyraakis F, Bidon-Chanal A, Luque FJ & Viappiani C (2013) Ligand migration through hemeprotein cavities: insights from laser flash photolysis and molecular dynamics simulations. *Phys Chem Chem Phys* **15**, 10686–10701.
- 91 Antonini E & Brunori M (1971) Hemoglobin and Myoglobin in Their Reactions With Ligands. North Holland Publishing Co., Amsterdam.